Reconstructing Unseen Spaces in Collapsed Structures for Search and Rescue Via Deep Learning-Based Radargram Inversion

Da Hu, Junjie Chen, Shuai Li*

Department of Civil and Environmental Engineering, The University of Tennessee, Knoxville, TN, USA
Department of Real Estate and Construction, The University of Hong Kong, Hong Kong, China

Abstract

This paper developed a novel deep learning-based approach to processing ground-penetrating radar (GPR) radargrams to reconstruct the occluded interior spaces of collapsed structures and extract essential information such as survivable void spaces to assist search-and-rescue operations. The proposed method innovatively exploits a generative adversarial network (GAN) to augment synthetic GPR training data and an end-to-end deep learning model to invert a GPR radargram to a permittivity map of the cross-section that can be further interpreted to reconstruct the interior scenarios of collapsed structures. First, to address the lack of training data with correct labels, synthetic GPR radargrams were generated from simulated scenarios of collapsed structures. The GAN was applied to augment the realism of synthetic GPR radargrams for training, providing a new mechanism for preparing and augmenting data that is difficult to collect from a real disaster site. Second, instead of detecting and segmenting nonintuitive features in GPR radargrams, a new encoder-decoder structure was trained using the augmented GPR radargrams to directly reconstruct permittivity maps corresponding to the cross-sections of collapsed structures. The visual Turing test indicated that the GAN substantially improved the realism of synthetic GPR radargrams. The proposed GPR inversion method achieved an R^2 value of 0.93, a Mean Absolute Error (MAE) of 0.73, and a Structural Similarity Index Measure (SSIM) of 0.95 in inferring the material permittivity from synthetic radargrams. The predicted permittivity map was further used to identify void spaces, achieving an F1 score of 64.34%, a precision of 63.06%, and a recall of 71.84% at the pixel level. On the augmented radargrams, the network achieved an R^2 value of 0.76, an MAE of 1.49, and an SSIM of 0.89 in predicting the permittivity map. The void detection on augmented radargrams achieved an F1 score of 45.20%, a precision of 45.35%, and a recall of 53.99% at the pixel level. The feasibility of using the proposed inversion network to reconstruct permittivity maps from radargrams is also experimentally tested and demonstrated in simulations of two multistory building collapses.

Keywords: Collapsed Structures; Search and Rescue; Disasters; Deep Learning; Radar; Reconstruction.

1. Introduction

Natural and man-made disasters such as earthquakes and explosions can lead to the collapse of buildings or infrastructure, causing numerous deaths and injuries [1]. According to [2], 15% of disaster victims are trapped inside void spaces under collapsed structures. The number of those who are successfully rescued, however, is comparatively small despite great and heroic search-and-rescue efforts. For instance, a 12-story condominium in Surfside, Florida, partially collapsed on June 24th, 2021. The disastrous collapse caused 98 deaths, while only a few survivors were pulled out from the rubble [3]. The emergency responders were deployed to enter collapsed structures to conduct search-and-rescue operations, which put their lives in danger from exposure to hidden hazards and secondary collapse. In the September 11th, 2001, attacks, more

than 400 emergency responders were killed during the search-and-rescue mission [4]. Subsurface information like void space is critical to help responders quickly locate entrapped victims and avoid potential hazards. Unfortunately, such information remains unavailable, significantly impairing the efficiency of search-and-rescue operations.

Under current practices, first responders have adopted a number of technologies, such as the thermal camera and listening device, to locate buried victims. The effectiveness of these techniques, however, depends heavily on the first responders' knowledge and experience. For instance, the deployment of a listening device and a thermal camera requires responders to first identify a location with a high probability of containing buried victims. However, subsurface information is always hard to obtain due to limited sensing capability. To address this challenge, several studies have begun to examine using ground-penetrating radar (GPR) in subsurface information extraction at disaster sites. GPR is a well-established method for subsurface imaging and has been demonstrated to be effective in underground utilities mapping, bridge inspection, and geological structures detection. In the disaster search and rescue domain, GPR has been used to detect buried victims under rubbles [5]. However, the success of victim detection requires the GPR to be in close proximity to the victims and suffers from noisy background signals. In [6], an algorithm was developed to detect and characterize void spaces in disaster rubble from GPR radargrams. However, the analysis is not sufficient as it only considers lean-to collapse voids, making it difficult to generalize to other types of collapsed voids that are also typical, e.g., pancake-shape and A-shape. In addition, while the aforementioned methods can identify the existence of voids or buried victims, they fail to provide detailed information about the underground space's layout and interior structure.

Defined as the measurement of the electric polarizability of a dielectric, the permittivity of a material is a strong indicator of its belonging to a certain material category (e.g., water, wood, or concrete). For example, the permittivity of air is around 1, while that of concrete is more than 6 [7]. With a permittivity map of a subsurface space, it would then become straightforward to infer how different materials are distributed in an underground structure. For example, an area with a permittivity value of around 1 has a high probability of being a void space where a survivor could be entrapped. A permittivity of around 4, on the other hand, implies that there might be wood or other materials with relatively low strength in the corresponding area, which lacks sufficient support to ensure the stability of the collapsed structures and therefore requires additional caution when excavating [8].

When mapping a subsurface space with GPR, permittivity is the primary factor influencing the speed of electromagnetic wave transmission, and it directly determines the radargram features. Therefore, it is theoretically possible to inversely infer the permittivity map of a subsurface structure from its GPR radargram. There have been pioneering studies that tried to reconstruct permittivity maps from GPR radargrams based on deep neural networks [9,10]. These works, however, mainly involve detecting defects in the linings of tunnels, which tend to have relatively homogenous and uniform layouts. As a comparison, collapsed rubbles are more complex, with multilayer structures and heterogeneous material distribution. In addition, these studies directly link time-dimensional GPR radargrams to space-dimensional permittivity data, which could lead to an inaccurate depth estimation of the target. For instance, in [10], radargrams with a two-way travel time of 20 ns were linked to permittivity maps with a depth of 1 m for different permittivity backgrounds (i.e., 5, 10, and 15). Furthermore, deep learning networks were trained on synthetic datasets without realistic radargram signatures in these studies, which largely affects their performance in real applications.

There are two challenges in using GPR to penetrate occluded disaster rubbles and processing the collected radargrams to infer permittivity maps of collapsed structures. First, it is very difficult to collect GPR data in real disaster sites and correctly label the ground truths. To our best knowledge, there is no GPR dataset for collapsed structures and disaster sites, preventing the development of advanced deep learning methods for data processing and interpretation. Second, conventional signal processing-based methods and computer vision methods primarily focus on detecting and segmenting individual and nonintuitive features in GPR radargrams. Given the complexity of the interiors of collapsed structures, detecting obvious features and inferring the scenarios is very difficult. Previous studies aimed to detect known signatures of objects that have regular geometries, such as underground utilities [11–14], and to estimate their locations, dimensions, and other properties. However, void spaces and building wreckages are of irregular shapes, and their signatures in GPR radargrams can be of various shapes and completely unknown a priori. The inhomogeneous environment makes it almost impossible to recognize and characterize void spaces and other unknown objects from their signatures in GPR radargrams using conventional processing techniques.

To overcome these challenges, a deep neural network (DNN)-based GPR data inversion approach was proposed in this study and trained on synthetic GPR data augmented by a generative adversarial network to infer the interior layouts of collapsed structures from reconstructed permittivity maps. The permittivity map can provide critical information regarding unseen spaces such as survivable void spaces, which has the potential to improve the efficiency, safety, and response time of search-and-rescue operations. This section will be succeeded by a background review of GPR in search and rescue and GPR processing algorithms. Methodology, experiments and validation, and a case study are presented in subsequent sections. Finally, results are discussed, and conclusions are summarized.

2. Background review

2.1 GPR in search and rescue

GPR is a non-destructive technique that has been widely used in subsurface target detection and reconstruction, and it has been demonstrated to be an effective method. Many studies have developed methods to reconstruct a variety of subsurface targets, such as underground utilities [11–14], cracks [15,16], roots [17,18], and concrete rebar [19]. In the search and rescue domain, GPR has been proved to be feasible in the detection of mission persons buried in snow following avalanches [20]. The GPR system with a 900 MHz antenna was pulled by manpower on snow surfaces. This search technique is very time-consuming and unsuitable for rugged avalanche surfaces. In addition, this method is almost impossible to employ on a mountain slope, where avalanches mostly occur. To address these limitations, the GPR was mounted on aerial vehicles to take full advantage of the GPR technique in avalanche search and rescue. For instance, a semiautomatic detection algorithm was developed to recognize potential victims buried in snow via airborne GPR [21]. In this method, snowpack is manually extracted to remove the zone of snowpack in GPR data, which requires expertise in GPR data and is error-prone. Fruehauf et al. [22] improved this method to achieve approximately real-time victim detection. The method first utilized an active contour model to extract snowpack in the radargram automatically. The template-matching method was then used to detect hyperbolic features formed by buried victims in the radargram. However, these methods were mainly developed for avalanche victim detection and are not suitable for victims buried in disaster rubbles because of those environments' cluttered and heterogeneous nature.

To date, various studies have assessed the efficacy of GPR in detecting human vital signs during urban search and rescue. For instance, in [23], a numerical modeling approach was adopted to study the feasibility of GPR in buried victim detection under a complex subsurface situation. The results showed the potential of the GPR technique in trapped victim detection under collapsed buildings. In the research conducted by Cist et al. [5], GPR was demonstrated to be applicable in detecting survivors' motion and breathing in rubble piles. More recently, Yang et al. [24] proposed a novel method to identify and locate human vital signs from radar-received signals based on permutation entropy (PE) and an ensemble empirical mode decomposition (EEMD) algorithm. Yan et al. [25] developed a Golay complementary coded system to detect quasi-static trapped victims under collapsed structures. The system consisted of stationary and scanning operating modes that were designed for nonperiodic strong respiration and quasiperiodic weak respiration, respectively. It should be noted that these victim-detection methods require leaving the GPR antenna static for a certain period. Furthermore, these methods require placing the GPR above the trapped victims, which is difficult to achieve in cluttered disaster sites. Identifying voids in structural collapses can pinpoint locations with potentially trapped victims, which can facilitate the deployment of victim-detection radar. A number of studies [6,26–28] have attempted to detect and reconstruct invisible void spaces based on GPR signal characteristics. The main drawback of these studies is the inability to provide critical information such as interior layout and structure.

Another important issue to be considered for search-and-rescue applications is the safety of GPR for the trapped victims. GPR is widely considered to be a safe and nondestructive subsurface imaging technique. The existing literature indicated that electromagnetic emissions from GPR systems are commonly far below International Commission on Non-Ionizing Radiation Protection (ICNIRP)'s recommended maximum level of 1 mW/cm^2, which does not constitute a health impact on operating personnel [29]. However, since the GPR antenna is radiating directly against trapped victims, the research conducted by Persico and Pajewski [30,31] suggested being careful to avoid any potential health impacts on the trapped victims in such applications. Therefore, the GPR antenna should be properly selected and tested before its deployment to disaster sites.

2.2 GPR data processing

Despite the wide usage and promising results in subsurface imaging of GPR, it remains a challenge to automate GPR data processing. In previous research, a variety of signal-based automatic algorithms have been developed to address this challenge. For instance, Wang et al. [32] developed an algorithm based on partial differential equations for hyperbola detection in GPR images. A template-based method was then used to identify the hyperbolic peak which represents the rebar location in a concrete bridge deck. In [33], a template-matching algorithm was also used to estimate the radius, buried depth, and horizontal location of cylindrical objects detected by GPR. However, the performance of the template-based method depends on the handcrafted threshold, and the method is sensitive to noise. Dinh et al. [34] developed a migration-based automated rebar picking method based on the Limited and Simplified Hyperbolic Summation technique. However, this method is only suitable for cylindrical objects with significant hyperbolic features.

The Full Waveform Inversion (FWI) method for seismic data has been adapted for GPR data to estimate subsurface properties. For instance, a Bayesian FWI was developed to detect and characterize subsurface structure defects using cross-hole GPR data [35]. The method integrated a two-dimensional finite-difference time-domain simulator, Markov chain Monte Carlo

simulation, and discrete cosine transform. Feng et al. [36] proposed an improved FWI method based on total variation regularization to estimate subsurface permittivity and conductivity for tunnel lining defect reconstruction. In their method, the total variation constraint and multiscale inversion approach were integrated to find the global optimal value. The FWI method has also been used to estimate layer thickness and properties of pavement structure using GPR data [37]. However, the inversion accuracy of FWI methods depends on initial model selection and may get stuck in local optima.

Machine learning techniques have been used to detect targets from GPR data. Kaur et al. [38] integrated the Support Vector Machine (SVM) classification method with histogram gradient features to detect rebar hyperbolic signatures from GPR radargrams. Harkat et al. [39], developed a multi-objective genetic algorithm to recognize hyperbolic features in the radargrams. The algorithm utilized a binary classifier with a neural network radial basis function to locate the target using high-order statistic cumulant features. Giannakis et al. [40] proposed a machine learning scheme to estimate the diameter of reinforcing bars in concrete structures using GPR. The proposed detection scheme consists of two neural network regression models and the random forest method. The main drawback of machine learning methods is that the detection performance relies on selected features, which is not applicable for cluttered field GPR data at disaster sites.

Much of the current literature on GPR data processing pays particular attention to Convolutional Neural Network (CNN) with the advancement of computational power. In the method proposed by Hou et al. [41], a Mask RCNN-based method was adapted to detect and segment rebar features in GPR radargrams. Their method introduced a novel loss function called distance-guided intersection over union to improve segmentation accuracy. Dinh [42] developed a CNN-based algorithm to localize and detect rebars from GPR data of concrete bridge decks. Hou et al. [43] adopted a Mask Scoring RCNN architecture to detect and segment plant roots from GPR radargrams. The anchor shape ratios were optimized to maximize the root signature detection. However, these methods were developed for cylindrical objects which appear as significant hyperbolic features in radargrams. Subsurface structures at disaster sites are more complex than simple cylindrical objects. More recent studies developed CNN-based inversion networks to reconstruct permittivity maps from GPR radargrams. This includes Liu et al. [9], in which authors proposed a trace-to-trace encoder-decoder network to directly map the GPR data to the corresponding permittivity map. The proposed network was demonstrated to be effective in reconstructing tunnel lining defects from radargrams. Ji et al. [10] developed a CNN-based permittivity inversion network (PINet) for permittivity map reconstruction from GPR data. A global feature encoder is incorporated to learn the spatial alignments between GPR radargrams and inverted permittivity maps. The shapes, locations, and permittivity of tunnel defects can be reconstructed using the PINet. The main drawbacks of these deep learning-based inversion methods have been discussed in the introduction section. This study aims to address these limitations.

3. Methodology

Fig. 1 presents an overview of the proposed framework for subsurface reconstruction in disaster rubbles, which consists of three steps. First, the gprMax simulator [44] is used to generate synthetic GPR data. The numerical simulation can generate a large amount of GPR radargrams along with ground-truth permittivity maps to train the neural network. In real disaster sites, it is almost impossible to obtain ground-truth permittivity maps corresponding to GPR radargrams. In addition, a variety of collapsed structures can be simulated to provide data that is difficult to

collect in real disaster sites. Second, a Generative Adversarial Network (GAN) is trained to augment the realism of the synthetic GPR data. The GAN method can reduce the domain gap between synthetic and real GPR data and thus enhance the generalizability and capability of the trained model. Third, a Convolutional Neural Network (CNN) model based on the encoder-decoder structure is designed to invert GPR data into subsurface permittivity maps. The CNN model is adapted from the UNet architecture [45]. The network integrates the Atrous Spatial Pyramid Pooling (ASPP) module to capture multiscale GPR information by changing the size of the receptive field to capture surrounding trace features. The ASPP module is beneficial for GPR data inversion since neighboring traces of radargrams are typically correlated with each other. Each step is detailed in the following section.

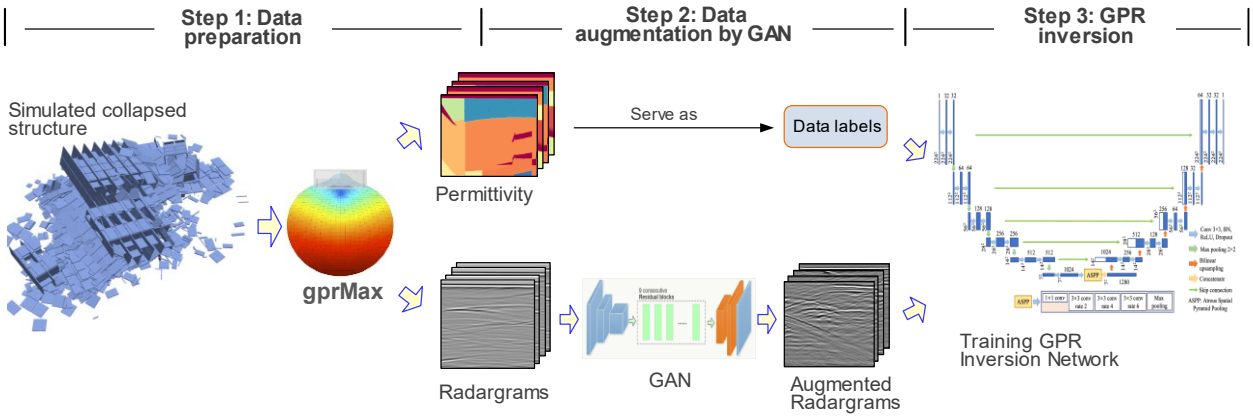

Fig. 1 Methodology overview

3.1 Data preparation

Numerical simulation is conducted to generate synthetic GPR radargrams as the training dataset. The gprMax is used as a simulator with a 350 MHz ricker pulse, which is well accepted for GPR simulation [44]. The 350 MHz antenna has a penetration depth of up to 10 m. Search-and-rescue efforts for entrapped victims under collapsed buildings generally start from the rubble's surface. In addition, entrapped victims have a higher survival probability within the top few meters. Therefore, the penetration depth of the 350 MHz antennae is suitable for subsurface imaging in the context of disaster rubbles. The subsurface structures under collapsed buildings are complex, with multiple layers which have different electromagnetic properties. The number of subsurface layers is randomly generated between 4 and 12. Each layer is further divided into a random number of sub-blocks. The relative permittivity of subsurface structures is randomly selected from 3 to 25. The void space is modeled as polygon and triangle shapes with a relative permittivity of 1. The size of the void is randomized and randomly placed within the simulated subsurface structures. To simulate a realistic collapse setting, subsurface structure, and shapes and sizes of void were generated to be as varied as possible. Each simulated permittivity map consists of 224 traces that are equal to a length of 2.24 m. The depth of simulated models is set to 6.7 m. Fig. 2 presents two examples of simulated permittivity maps.

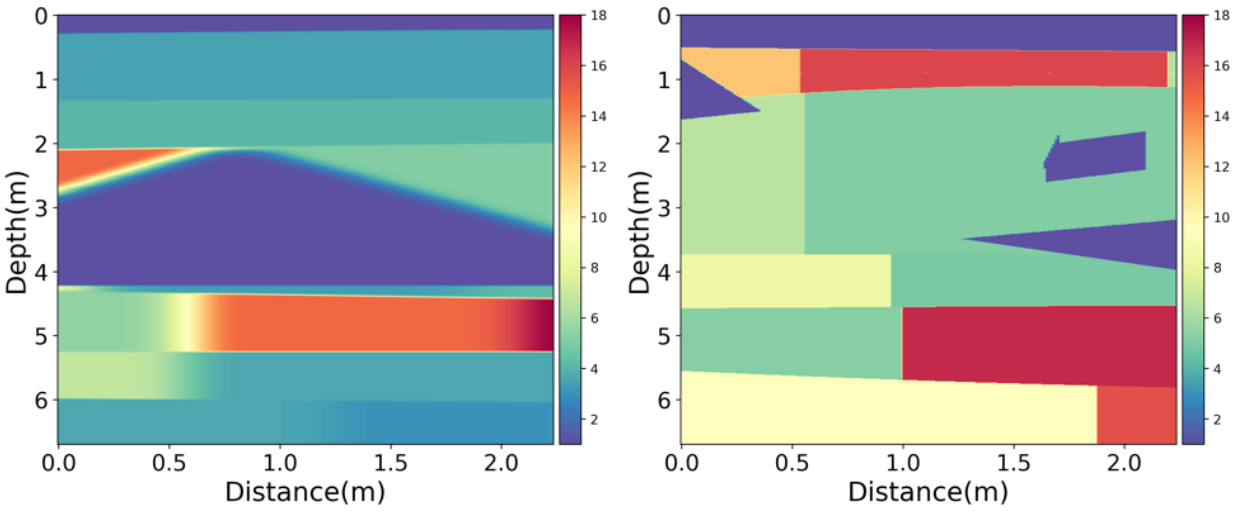

(a) (b)

Fig. 2 Example of two simulated permittivity maps.

The simulated subsurface models were in the spatial depth domain, which needs to be converted into the time depth domain to match simulated radargrams. Eq. (1) gives the conversion, where t represents two-way travel time in ns, d is the depth in m, ε is the relative permittivity, and C is the speed of light (3×10^8m/s).

$$t = \frac{2d}{C}\sqrt{\varepsilon} \tag{1}$$

The gprMax simulation spatial step is 0.01 m, and the time window is 2.35865e-11s. The number of iterations is set as 3,000. Each radargram is composed of 224 traces that are equal to a length of 2.24 m. The time-zero correction and exponential gain are applied to the radargram. The time-corrected radargram has an iteration of 2,715, which is equivalent to 64 ns. The samples for each trace are downsampled to 224. The first 64 ns of the simulated permittivity map are extracted to match the travel time of the simulated radargrams. The samples of the permittivity map are also downsampled to 224. A total number of 55,799 data pairs are generated. Each data pair consists of a subsurface permittivity map and a GPR radargram over that respective area. Fig. 3 presents two examples of subsurface permittivity maps and corresponding radargrams in the time-depth domain.

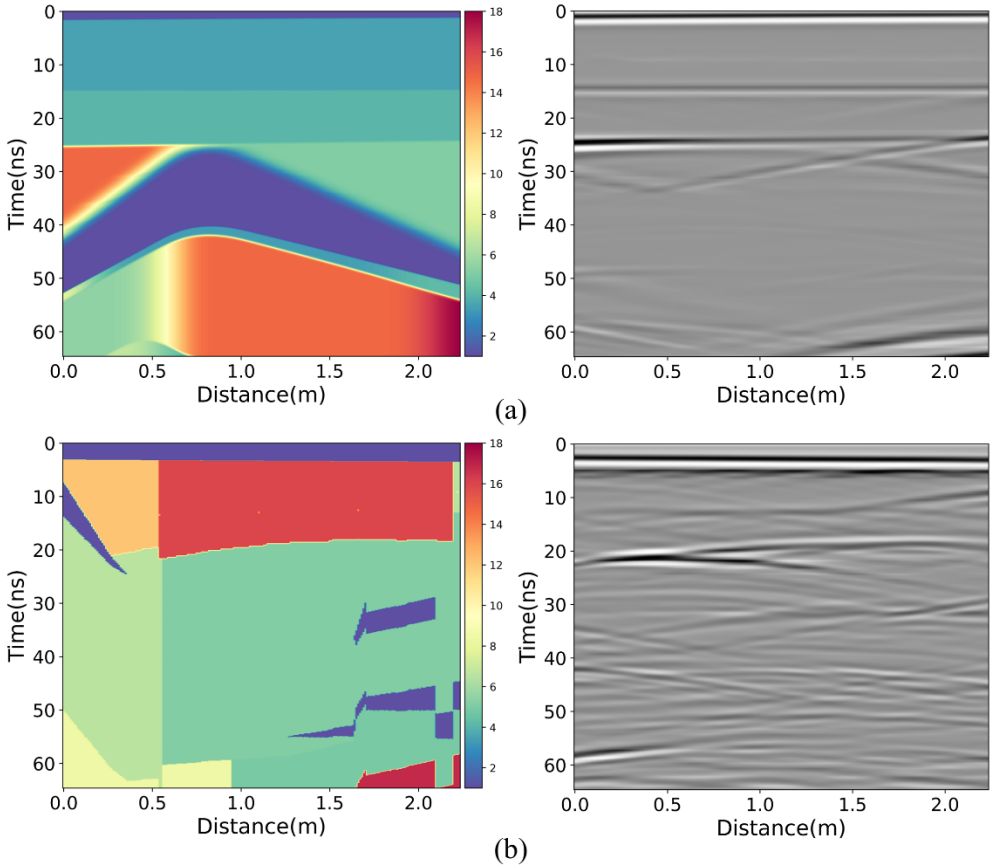

Fig. 3 Examples of simulated permittivity maps and radargrams in the time-depth domain.

3.2 Data augmentation with GAN

Despite the convenience of simulation, there is a certain level of deviation between the simulated results and the real GPR radargrams. Training the permittivity prediction networks on the synthetic GPR radargrams provided by simulation tools might hinder the generalizability of the resulting model to real scenarios in the future. Therefore, the generative adversarial network (GAN) technique is used to enhance the realism of the simulation results.

CycleGAN [46], a GAN framework for unpaired image-to-image style translation, has demonstrated solid performance in rendering simulated images with photorealistic texture while still preserving the original contents [47]. Fig. 4 shows the CycleGAN structure for GPR radargram augmentation. The model involves two types of deep neural networks (i.e., Generators and Discriminators) that are mutually adversarial in a zero-sum game theory: while one of the Generators takes the synthetic radargrams simulated by gprMax as input and produces realistic radargrams after refinement (referred to as augmented radargrams thereafter) as output, one of the Discriminators is fed both augmented and real radargrams and distinguishes whether a given sample is real or fake. The Generator and Discriminator form a composite model (denoted by Composite Model #1) that aims to generate augmented GPR radargrams with high realism. To ensure the augmented and synthetic radargrams can be paired up, Composite Model #2 is used, in which the Generator aims to generate synthetic radargrams, while the Discriminator is trained to distinguish the synthetic radargrams from their real counterparts.

The two composite models are trained simultaneously, after which the Generator of Composite Model #1 will be used separately for data augmentation. The collection of synthetic radargrams generated by the gprMax is used as input to the Generator network, which then processes and augments the radargrams with realistic details and texture applied. The output radargrams are not only visually similar to real data but also preserve the corresponding subsurface permittivity annotations that can be used for inversion model training in the next section.

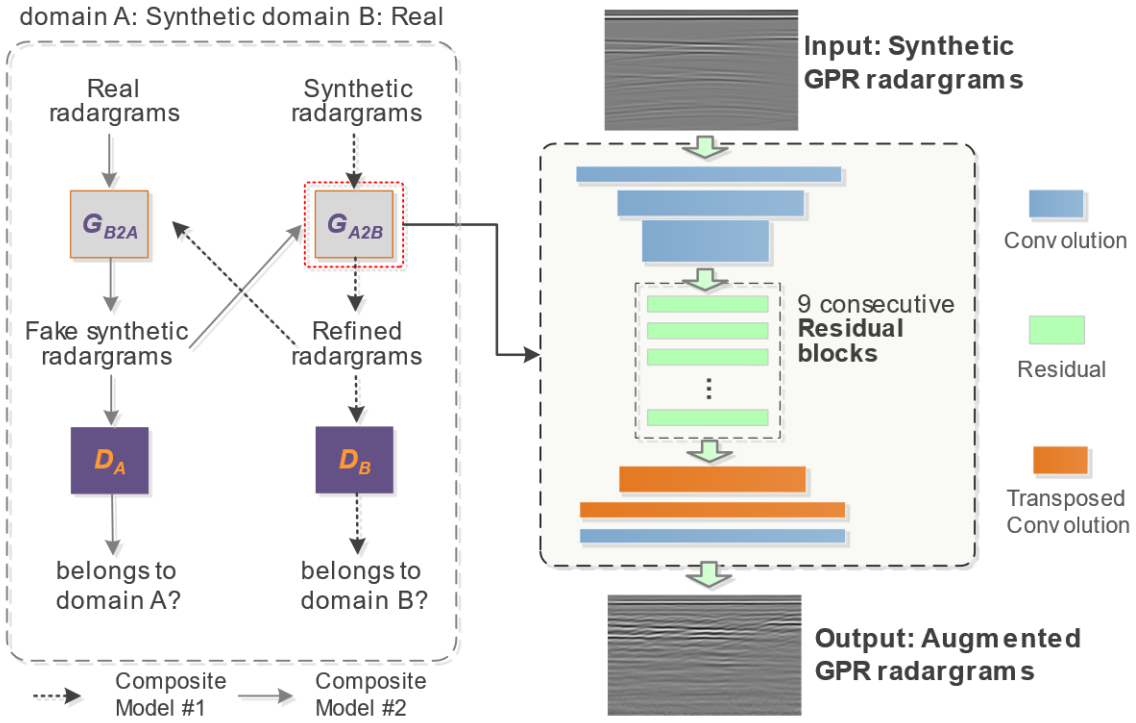

Fig. 4 Model structure of CycleGAN for GPR radargram augmentation.

3.3 GPR Inversion Network

Fig. 5 presents the architecture of the proposed network. The proposed deep learning network is adapted from the UNet architecture [45], which consists of three sections: contraction, bottleneck, and expansion. The radargram is first fed into the contraction section, which is composed of five convolutional blocks. Each block consists of two 3×3 convolution operations followed by 2×2 max pooling on feature maps. The spatial size of the feature map reduces to half, and the dimension doubles when the network progresses from shallow to deep blocks.

The bottleneck layer consists of a 3×3 convolutional operation, Atrous Spatial Pyramid Pooling (ASPP), and a bilinear upsampling layer. The ASPP module is applied to extract multi-scale features using multiple parallel filters with different rates. This process can improve inversion accuracy with the ability to account for neighboring traces of a radargram, which is important to capture object features with different scales. This is because the GPR antenna sends electromagnetic waves in a cone shape, and thus neighboring traces are correlated to each other in a radargram. The ASPP module contains a 1×1 convolution layer, three 3×3 convolution layers, and global average pooling. The sampling rates of the four convolution layers are 1, 2, 4, and 6, respectively. The batch normalization and ReLU activation layer are added, followed by each convolution layer and pooling layer. The output of a single layer from the ASPP module is 256 channels. The five layers are concatenated together with 1,280 channels. Subsequently, a

1×1 convolution with 512 output channels is applied to the concatenated layer to obtain a high-level feature map.

The expansion layer is used to recover the spatial size of the feature map to the size of input radargrams. The expansion section is composed of five convolutional blocks which correspond to the contraction section. Each block consists of two 3×3 convolution operations and a bilinear upsampling. The size of feature maps doubles, and channel numbers decrease with increasing expansion blocks. The low-level features are concatenated to corresponding high-level features to ensure features learned from the contraction section can be used for inversion. The number of channel numbers is the same for low-level and high-level features. Finally, the feature map is fed into another 3x3 convolutional operation. The spatial size of the output feature map is equal to input radargrams and the channel number is 1.

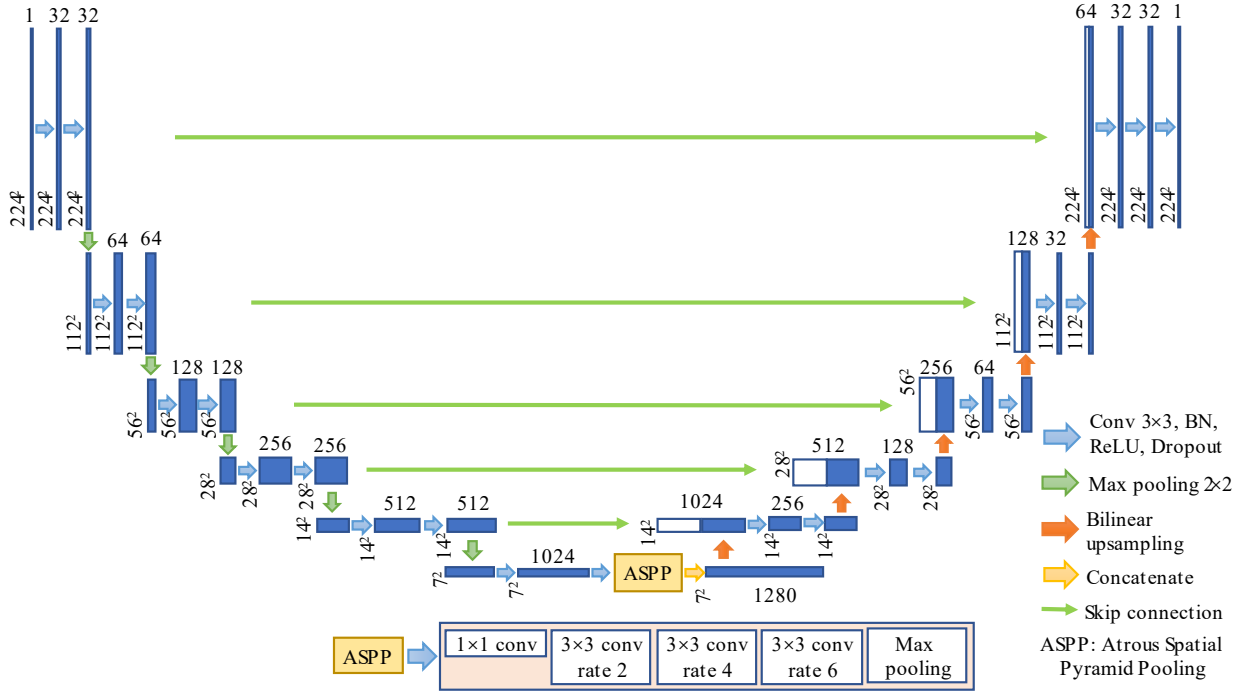

Fig. 5 Architecture of the proposed GPR inversion network

4. Experiments and validation

4.1 Data augmentation

4.1.1 Implementation details

The network was trained on a Linux workstation with Dual NVIDIA Quadro P5000 using the PyTorch backend [48]. A batch size of 1 and a learning rate of 0.0002 were used to train the network. The learning rate started to decay linearly after 100 training epochs. In addition, a pool size of 50 was set to store augmented radargrams. The real GPR radiograms were collected using GSSI 350MHz antenna. A total number of 5,748 GPR radargrams were collected, and each radargram consisted of 224 traces. A set of 5,748 synthetic GPR data was randomly selected from 55,799 GPR-simulated radargrams to train the CycleGAN model. The sizes of the real and synthetic GPR data are both resized to 224×224. The network stops training when augmented radargrams look visually similar to real radargrams.

4.1.2 Visual Turing test

The visual Turing test is adopted to evaluate to which level the CycleGAN has improved the realism of the synthetic GPR radargrams. Specifically, we randomly sampled 150 images from the “Real,” “Augmented,” and “Synthetic” datasets, respectively. The samples were then outsourced to the Amazon Mechanical Turk platform, where workers are required to rate whether a given radargram is “Real” or “Fake.” Each radargram was rated by five workers. Before the rating started, the workers were trained with six examples. This process aims to enable the workers to get familiar with GPR radargrams as well as the task. Note that the ground–truth labels for the “Augmented” and “Synthetic” datasets are both “Fake.”

Table 1 shows the results of the visual Turing test. It can be observed that, compared with the original synthetic dataset (only 10.7% misjudged as “Real”), the proportion of samples misjudged as “Real” was significantly increased to 27.3% after CycleGAN augmentation. This proportion is even greater than the 22.7% of real radargrams rated as “Real”. The results indicate that the realism of the synthetic GPR data has been substantially improved, which then led to greater confusion among the workers in distinguishing the “Real” and “Fake” samples.

Table 1 Quantitative results of Visual Turing Test

Dataset	Rated as “Real”		Rated as “Fake”	
	Number	Ratio (%)	Number	Ratio (%)
Real	34	22.7	116	77.3
Augmented	41	27.3	109	72.7
Synthetic	16	10.7	134	89.3

Fig. 6 presents examples of CycleGAN-augmented radargrams in comparison to synthetic radargrams. The augmented radargrams successfully learned realistic signal noisy features from real radargrams while preserving reflection signatures from subsurface structures.

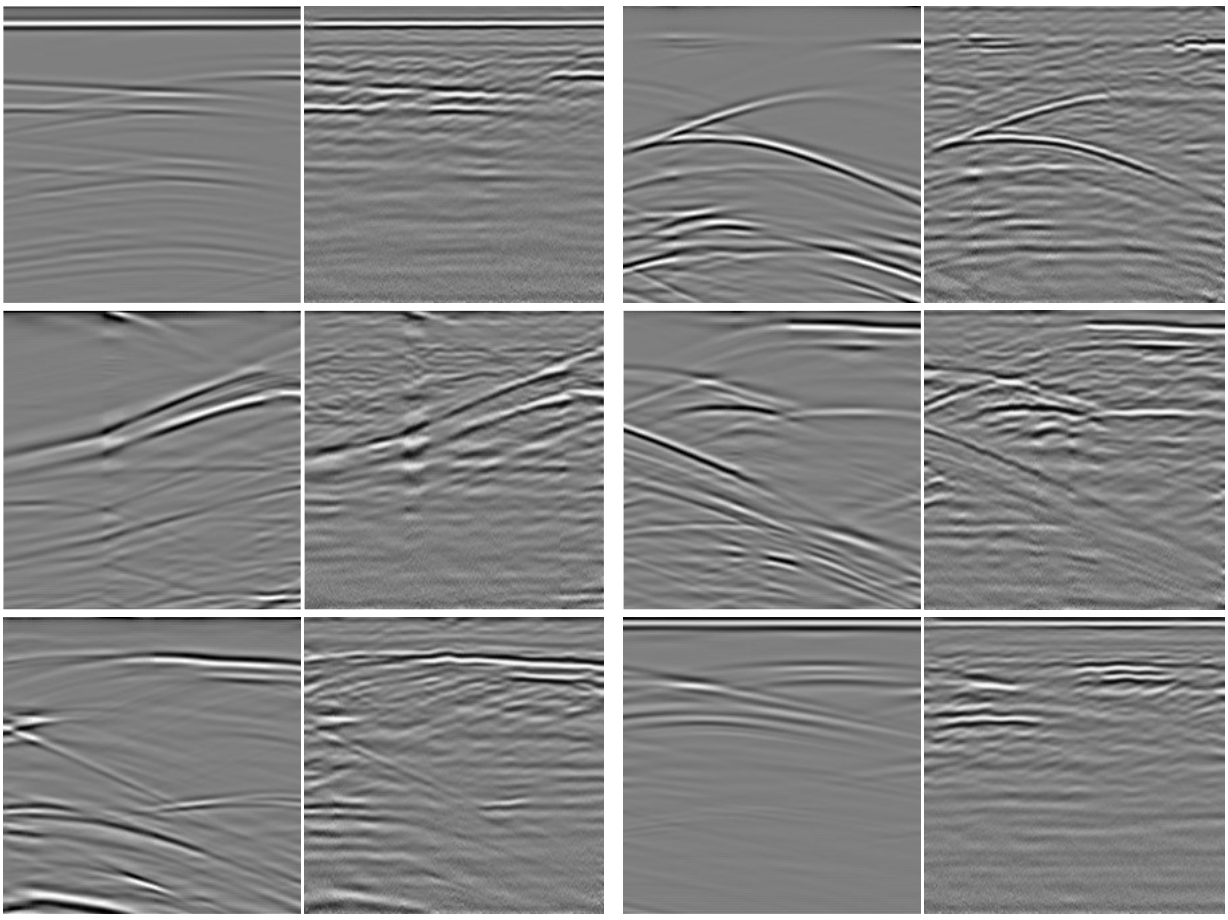

Fig. 6 Comparison between original radargrams and augmented radargrams.

4.2 GPR inversion

4.2.1 Implementation details

The dataset contains a total of 55,799 data pairs and radargrams that were augmented by the CycleGAN network. The dataset was randomly split into a training set (80%), a validation set (10%), and a testing set (10%). In addition, a small dataset that contains a total of 1,017 radargrams and corresponding permittivity maps were collected from rubbles of simulated collapsed structures. The small dataset is used to fine-tune the network for its application in realistic structural collapse scenarios. The RMSProp optimizer was adopted to train the network. The mean squared error loss function was selected. The initial learning rate is set to 0.0001, with PyTorch's ReduceLROnPlateau scheduler using max mode with patience of 20. The batch size is 64. The early stopping technique was used to reduce overfitting and increase the generalizability of the trained network. Specifically, the training set is used to train the network, and the trained network is evaluated on the validation set. If the performance of the network does not increase for 20 epochs, the network will stop training and save the best model on the validation set.

4.2.2 Metrics

In this study, three evaluation metrics, i.e., Structural Similarity Index Measure (SSIM) [49], *R*-squared (R^2), and Mean Absolute Error (MAE), are selected. The SSIM is an image similarity

comparison metric considering a variety of factors such as structural information, brightness, and contrast ratio. The SSIM metric is defined in Eq. (2), where μ_x and μ_y are averages of the ground truth and predicted permittivity map, respectively; σ_x and σ_y are variances; σ_{xy} is the covariance; and c_1 and c_2 are constants to stabilize the denominator.

$$\mathrm{SSIM}(x,y) = \frac{(2\mu_x\mu_y+c_1)(2\sigma_{xy}+c_2)}{(\mu_x^2+\mu_y^2+c_1)(\sigma_x^2+\sigma_y^2+c_2)} \tag{2}$$

R^2 is used to measure how predicted permittivity fit the ground-truth permittivity map. The R^2 value ranges from 0 to 1, where 1 means the prediction is perfectly aligned with the ground truth. Eq. (3) defines R^2, where x_i and y_i are the ground truth and predicted permittivity map, and n is the batch size.

$$R^2 = 1 - \frac{\sum_{i=1}^{n}(x_i-y_i)^2}{\sum_{i=1}^{n}(x_i-\mu_x)^2} \tag{3}$$

The MAE measures the difference between each element in the predicted and ground-truth permittivity map. It is defined in Eq. (4).

$$\mathrm{MAE} = \frac{1}{n}\sum_{i=1}^{n}|y_i - x_i| \tag{4}$$

4.2.3 GPR inversion results

This section discusses the GPR inversion results. Fig. 7 presents the variation of the three metrics SSIM, R^2, and MAE, over epochs on the validation set of synthetic and augmented radargrams. As the epoch number increases, the MAE decreases, and the R^2 and SSIM increase on both validation sets. The network converges quickly and becomes stable after around 60 epochs.

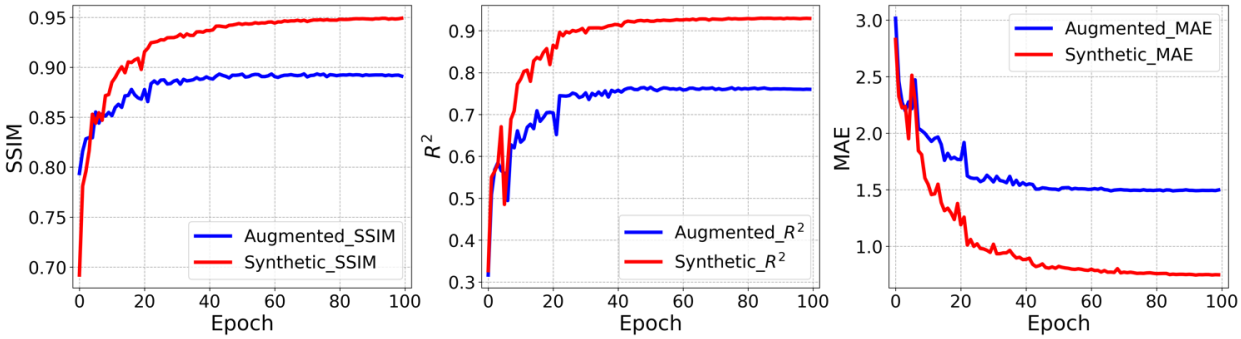

Fig. 7 SSIM, R^2, and MAE over epochs during training on the validation set of synthetic and augmented radargrams

Table 2 presents a comparison of synthetic and augmented radargrams. The best performances achieved on the validation set of augmented radargrams are 0.89, 0.76, and 1.49 for the SSIM, R^2, and MAE metrics, respectively. For the synthetic radargrams, the inversion network achieved better performance, with an SSIM of 0.95, an R^2 of 0.93, and an MAE of 0.73. This is because synthetic and augmented radargrams are associated with the same permittivity map. However, augmented radargrams learn realistic signal features using the GAN, which becomes more cluttered with random noise. Thus, the inversion task is more challenging on the augmented dataset compared to synthetic dataset. Note that the inversion model trained on augmented radargrams can be better generalized for real-world applications by learning realistic GPR radargram features.

Table 2 Model performance on synthetic and augmented radargrams

Metric	SSIM	R^2	MAE
Synthetic	0.95	0.93	0.73
Augmented	0.89	0.76	1.49

Fig. 8 presents example inversion results on the testing set of CycleGAN-augmented GPR radargrams. The permittivity values inverted by the network are in good agreement with the ground-truth permittivity map. The predicted permittivity map correctly reconstructs subsurface structures, which can provide important information such as void shape and location to first responders.

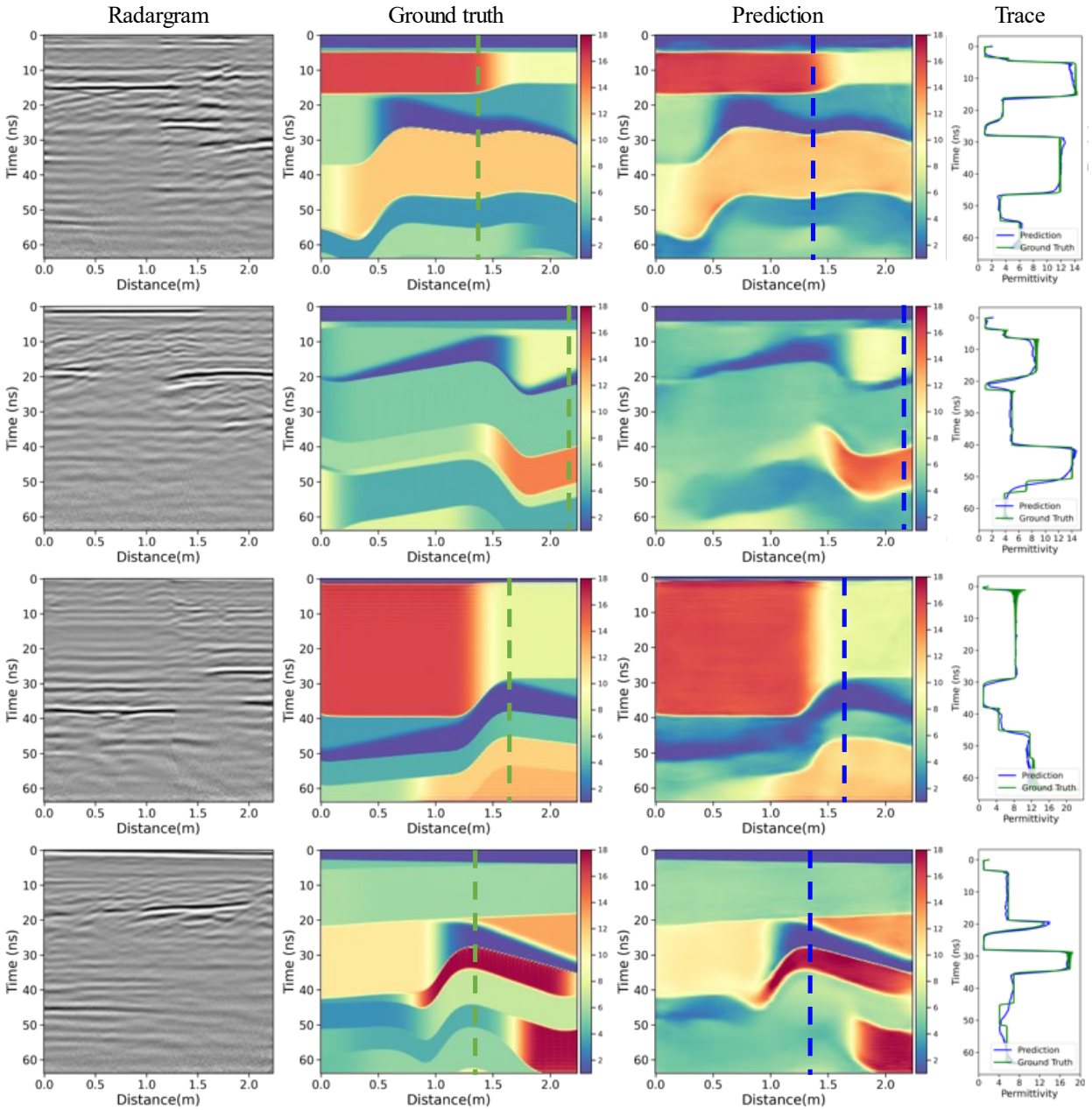

Fig. 8 Example results of GPR inversion network on the testing dataset of augmented radargrams. A single trace with relative permittivity values is randomly selected in predicted and ground-truth permittivity maps for each example.

The uncertainty of the inversion network is estimated using the Monte Carlo dropout proposed in [50], which can learn the predictive distribution. In the inference, a different set of neurons are dropped out in each layer randomly according to the layer's dropout rate. Therefore, the model is slightly different in each inference. The network is trained with a dropout rate of 0, which will not remove any neurons in the training process. During the inference, the dropout rates of 0.05, 0.1, and 0.2 are investigated, with a total of 1,000 runs for each rate. The variance of model prediction can be estimated in Eq. (5), where σ is the standard deviation, N is the total number of inferences, θ is the average predicted permittivity, and x_i is the predicted permittivity.

$$\sigma^2 = \frac{\sum_{i=1}^{N}(x_i-\theta)^2}{N} \tag{5}$$

Fig. 9 presents example results of standard deviations of the network prediction with different dropout rates. The radargram is randomly selected from the testing set of augmented radargrams. The results indicate that a higher dropout rate leads to a greater standard deviation of predicted permittivity values. A large standard deviation value represents a prediction with high variability. The prediction with the standard deviation can be used to capture the uncertainty of the network prediction.

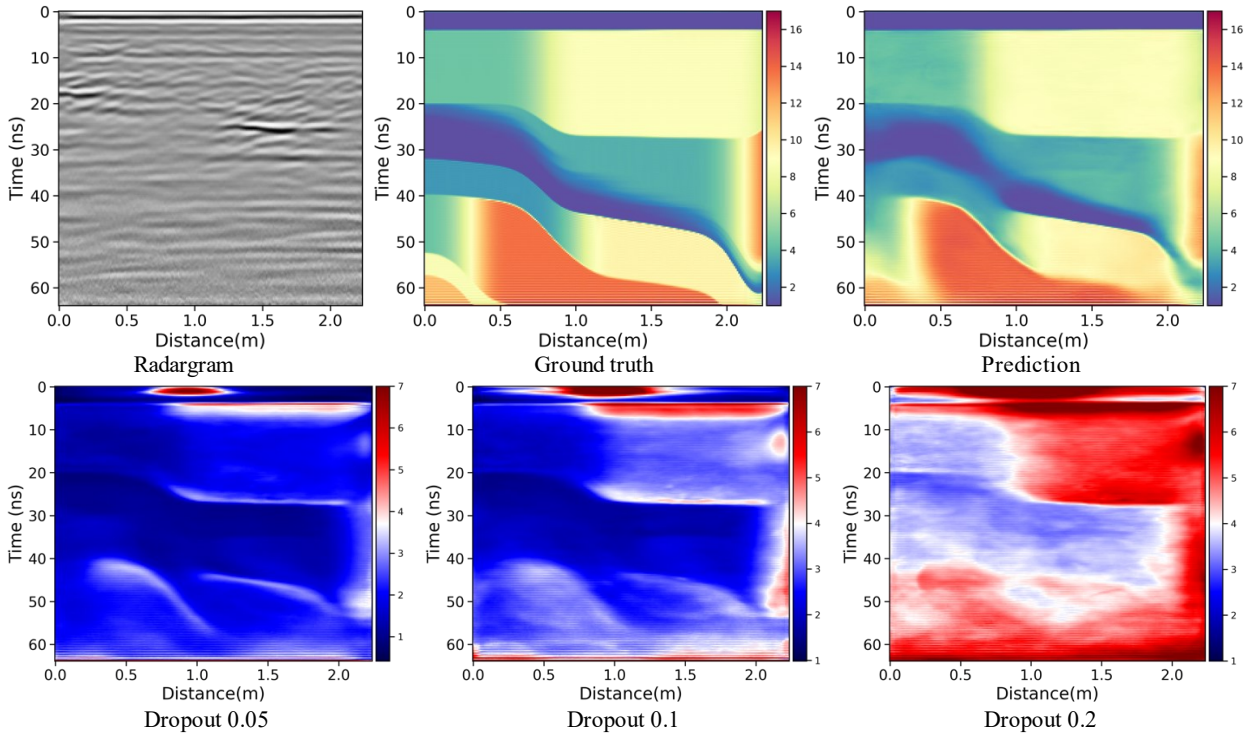

Fig. 9 Standard deviation of predicted permittivity map. The second row is the standard deviation with different dropout rates.

4.2.4 Void detection results

Since void spaces are critical for first responders to searching for trapped victims, the performance of the inversion network in predicting voids is further evaluated based on precision, recall, and F1 score. In particular, precision measures the ratio of accurately predicted pixels to all predictions; recall measures the ratio of accurately predicted pixels to all pixels in the ground truth; F1 score is the harmonic average of recall and precision. The testing sets of synthetic and augmented radargrams are used for the evaluation with a total of 5,579

radargrams along with permittivity maps. The permittivity maps without voids and with small voids are excluded, resulting in a total of 4,516 pairs of data.

Theoretically, the relative permittivity of the void should equal 1 in the permittivity map. However, the value could be either greater or smaller than 1 in the predicted permittivity map. This is because the proposed inversion network is used to predict permittivity maps from GPR radargrams, which could lead to an offset of relative permittivity for voids depending on radargram features. Therefore, the areas with relative permittivity values smaller than a specific permittivity threshold in the predicted permittivity map could be void spaces. Note that increasing the permittivity threshold for the void can increase the number of true positives but also lead to an increase in false positives. In this study, relative permittivity thresholds from 1.1 to 2.5 are investigated. Fig. 10 shows the variation of precision, recall, and F1 under different permittivity thresholds on synthetic and augmented radargrams. On the synthetic radargrams, the results indicate that the F1 score reaches a maximum of 64.34% when the permittivity threshold is set to 1.5. At the threshold of 1.5, the precision and recall are 63.06% and 71.84%, respectively. With respect to augmented radargrams, the maximum F1 score is 45.2% at the threshold of 2. The precision and recall are 45.35% and 53.99% at the pixel level, respectively. The promising results indicate the inversion network's ability to detect voids from GPR radargrams.

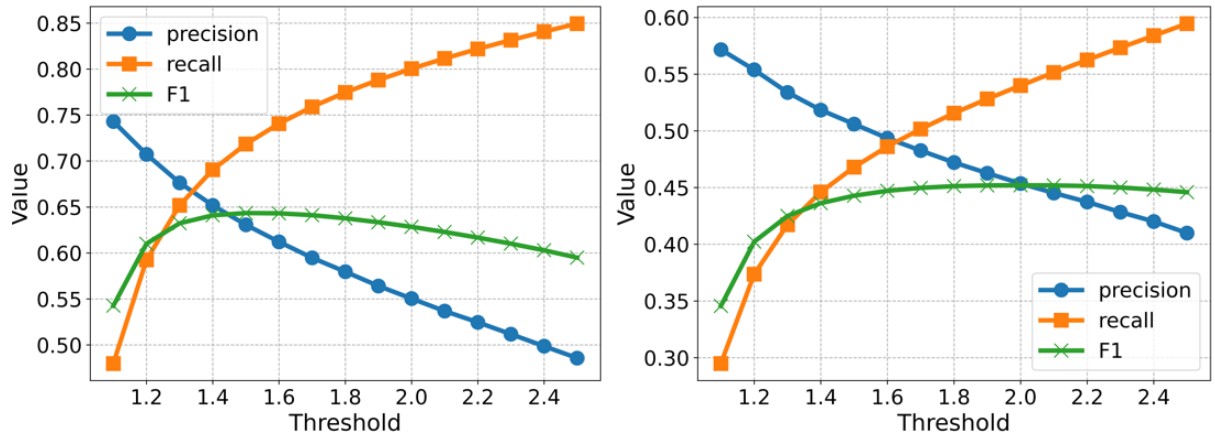

(a) Synthetic (b) Augmented

Fig. 10 Precision, recall, and F1 variation with relative permittivity thresholds on synthetic and augmented radargrams

5. Case study

The performance of the network is qualitatively evaluated on simulated radargrams collected from collapsed structures generated using a building collapse simulator named the Bullet Constraints Builder (BCB) [51]. The BCB is a suitable tool to simulate the effects of major structural deficiencies in composite reinforced concrete structures such as incapacitated load-bearing elements such as pillars, walls, beams, slabs, etc. The toolset is integrated in conjunction with the Bullet physics engine in the software Blender. The BCB has been validated by comparing it to a few real collapses of buildings, in which the simulation results showed good agreement with the real-world collapse shapes [51]. A multistory apartment building collapse caused by an earthquake was simulated using the BCB tool. Fig. 11 presents the 3D model of the collapsed structure.

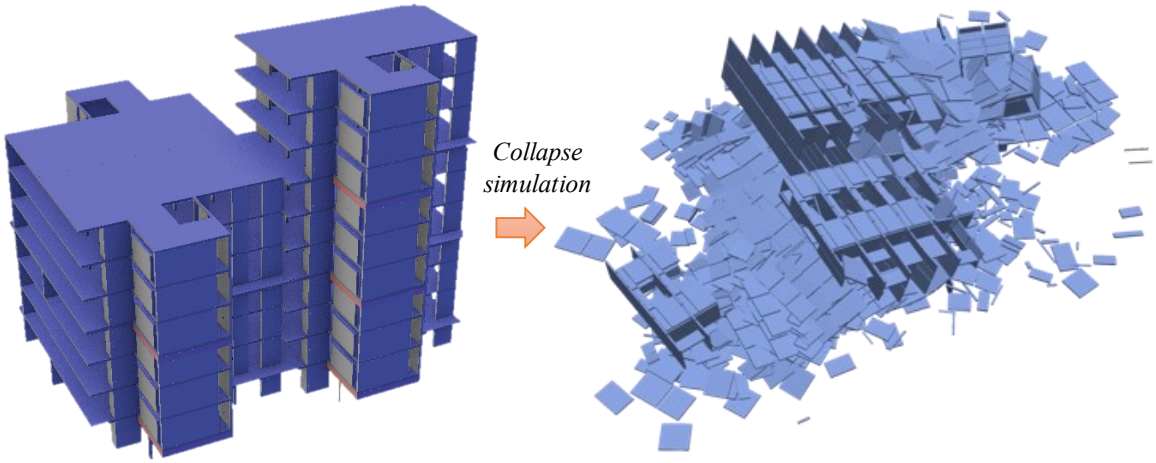

Fig. 11 3D model of the collapsed structure generated using the BCB

Two target locations with potential trapped victims are selected from the collapsed structure, and corresponding cross-sectional models are extracted. The permittivity values for subsurface structures in the cross-sectional model are randomly sampled from 4 to 16, which is consistent with permittivity of typical building materials [7]. Fig. 12 shows two target locations and their corresponding cross-sectional permittivity maps. The horizontal distance of the cross-sectional model is 2.24 m, and the depth is 6.9 m. As indicated, the two cross-sectional models are both irregular and cluttered with void spaces, which can be considered as the pancake void. Pancake collapses occur frequently after major earthquakes or severe damage to the building, which makes conducting search-and-rescue operations dangerous and difficult. The building collapse that happened in Miami, Florida, was a pancake collapse, where emergency responders struggled to identify void spaces under the rubble to reach entrapped victims.

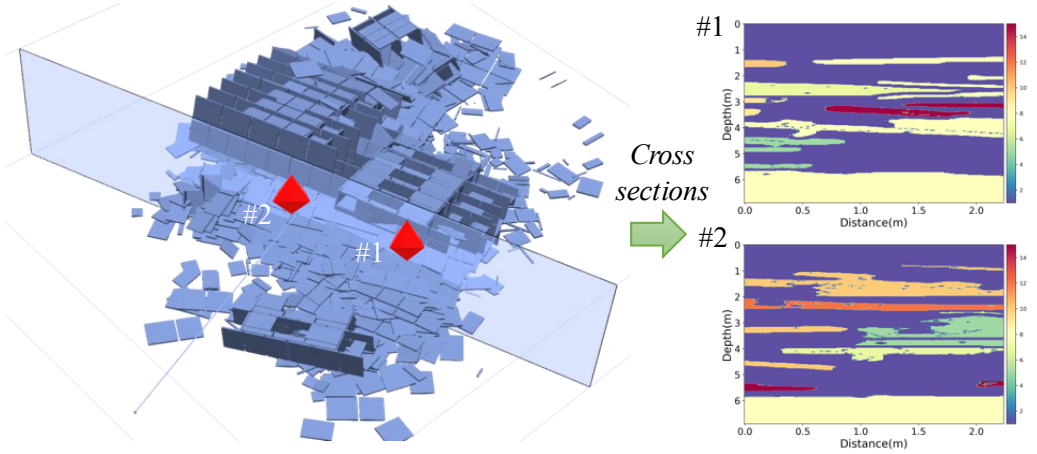

(a) Target locations (b) Permittivity map

Fig. 12 Target locations and corresponding permittivity maps

The cross-sectional model is then fed into the gprMax simulator using a 350 MHz antenna to generate synthetic radargrams. The simulation spatial step is set to 0.01 m, and the time window is 2.35865e-11s. The number of iterations is set to 3,000. The synthetic radargrams are preprocessed with time-zero correction and exponential time gain. The permittivity map is converted into the time-depth domain using Eq. (1). The synthetic radargrams after GAN

augmentation are fed into the network to predict the corresponding permittivity map. The GPR inversion results using the network are shown in Fig. 13. Note that the inverted permittivity map is smoothed using a Gaussian filter with a standard deviation of 3. The results indicate that large void spaces can be located in the inverted permittivity map. In particular, for the first target location, the inversion result can identify the two large voids that are close to the top and bottom in the permittivity map. For the second target location, the large void space located at the bottom can be identified in the predicted permittivity map. Some small voids can be also located, though they become noncontinuous in the predicted permittivity map. The results demonstrate that the network has the potential to be employed for subsurface reconstruction in complex disaster rubbles.

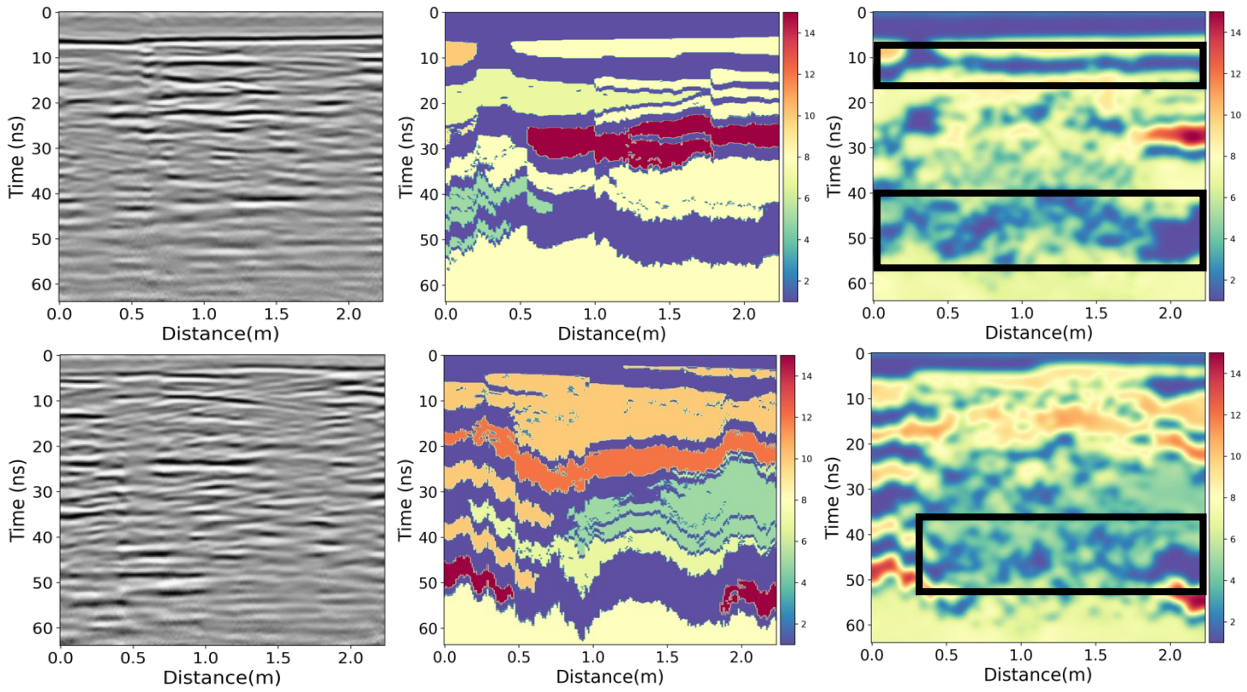

(a) Radargram (b) Ground truth (c) Prediction

Fig. 13 Inversion results of the radargrams collected at locations #1 and #2. The first row is for location #1, and the second row is for location #2.

6. Discussions

6.1 Comparison with state-of-the-art methods

Reconstructing subsurface interior scenarios in disaster rubbles provides critical information to first responders regarding subsurface conditions. In this study, we developed a deep neural network (DNN)-based GPR data inversion approach and trained it on CycleGAN-augmented radargrams to infer the interiors of collapsed structures from reconstructed permittivity maps. In [52], the as-built Building Information Model (BIM) was fed into a collapse simulation engine to simulate a variety of damage patterns of the building, which formed a virtual collapse structure database. The as-damaged exterior model was compared with the dataset, and the best-matching collapse structure was retrieved for use as the as-damaged interior model. However, the method required the as-built BIM of the damaged building, which cannot be obtained for most of the old buildings. Furthermore, the validity of the simulation engine is questionable for complex building structures such as those in the real world. Our solution is more robust and

reliable, which can provide in-situ information regarding subsurface interior scenarios. In addition, our method can be generalized to different types of collapsed structures and provide interior layouts and permittivity distributions, which have not been achieved in [6].

The CycleGAN network was innovatively applied to the synthetic GPR data to improve their realism while preserving signal features. In our study, 5,748 synthetic and real GPR radargrams were used to train the CycleGAN. The realism of the augmented radargrams is substantially improved as indicated by the visual Turing test. In [47], the authors used around 700 images from each domain, and the resulting proportions of samples rated as “Real” were 23% and 52% for the GAN-augmented and real dataset, respectively. In another study conducted by Maeda et al. [53], the respective proportions of samples rated as “Real” were 25% and 12% when the number of training images was 1,200. Compared to these studies, our network was trained with a much larger dataset, which has the potential to produce more robust performance. Furthermore, many studies have utilized synthetic GPR data to detect subsurface defects [9,10], rebar [54], and underground utilities [55]. The synthetic and real GPR data have different signal characteristics because real GPR data often suffer from noisy signals and signal scattering. However, these studies have not investigated the domain gap between synthetic and real GPR radargrams, which could hamper their application in real-world scenarios. The CycleGAN network utilized in our study can reduce the domain gap and thus promote developed algorithms to real-world scenarios.

6.2 Robustness of the inversion network

In real-world applications, GPR data often suffer from random noise that can affect the signal-to-noise ratio and blur useful signatures. In this section, we evaluate the robustness of our inversion network by predicting radargrams with random Gaussian noise. Specifically, random Gaussian noise with mean μ and standard deviation 0.5σ is added to the original radargram, where μ and σ are the mean and standard deviation of the original radargram, respectively. Fig. 14 shows example prediction results on radargrams with random Gaussian noise. The results indicate that predicted permittivity maps can properly reconstruct void spaces as well as interior layouts, which demonstrates the robustness of the proposed method.

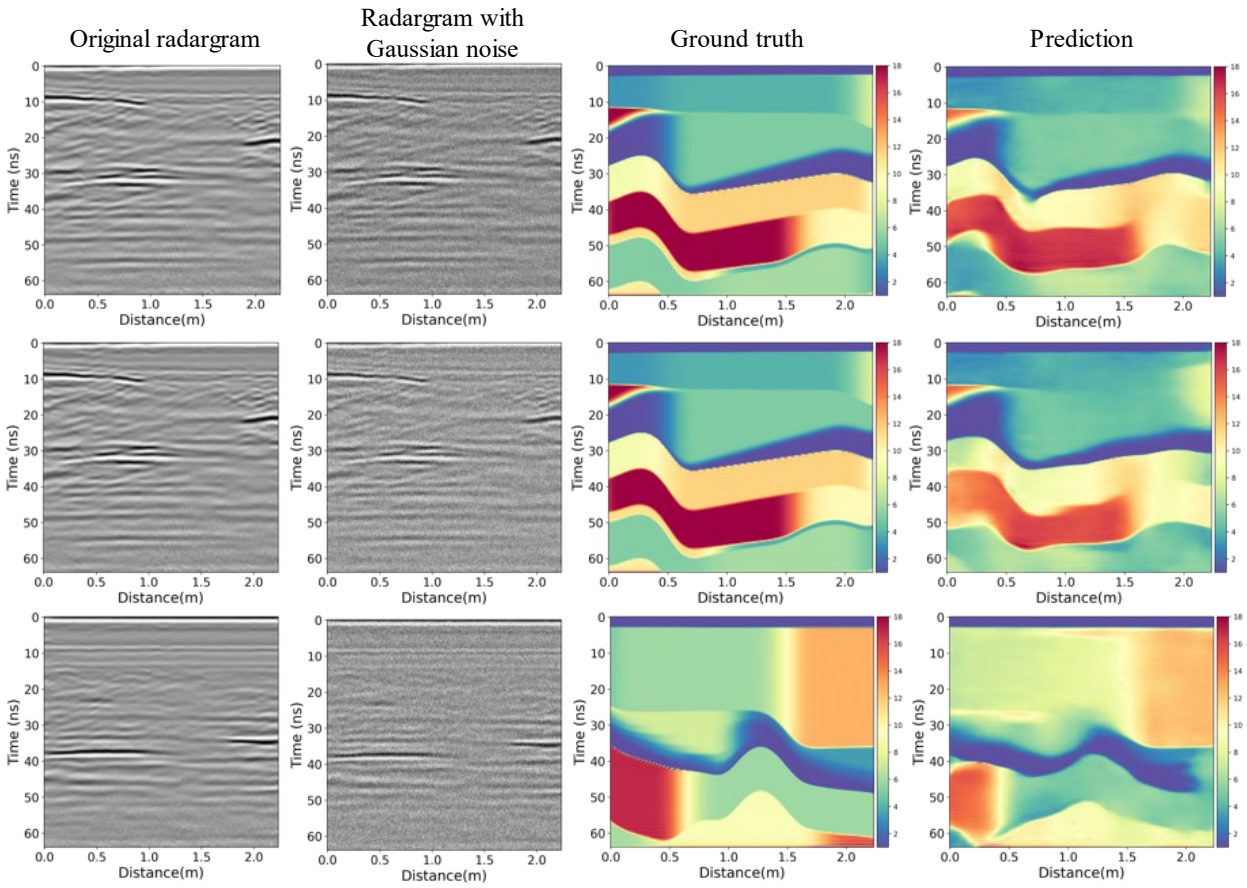

Fig. 14 Prediction results on radargrams with random Gaussian noise

To further assess the generalizability of the inversion network, the fine-tuned model is applied to a tall building collapse. Specifically, a total of 1,017 radargrams with ground-truth permittivity maps were collected from the collapsed structure in Fig. 11 to fine-tune the inversion network. The dataset was randomly split into a training set (90%) and a validation set (10%). The initial learning rate was set to 0.0001, with PyTorch's ReduceLROnPlateau scheduler using max mode with patience of 20. The batch size was 64. The loss function is mean squared error. The network will stop training when the loss value does not decrease for 10 epochs on the validation set. The best performance achieved on the validation set was used to perform inference on the new collapsed building. Fig. 15 shows the variation of SSIM, R^2, and MAE over epochs during the training stage on the training and validation sets.

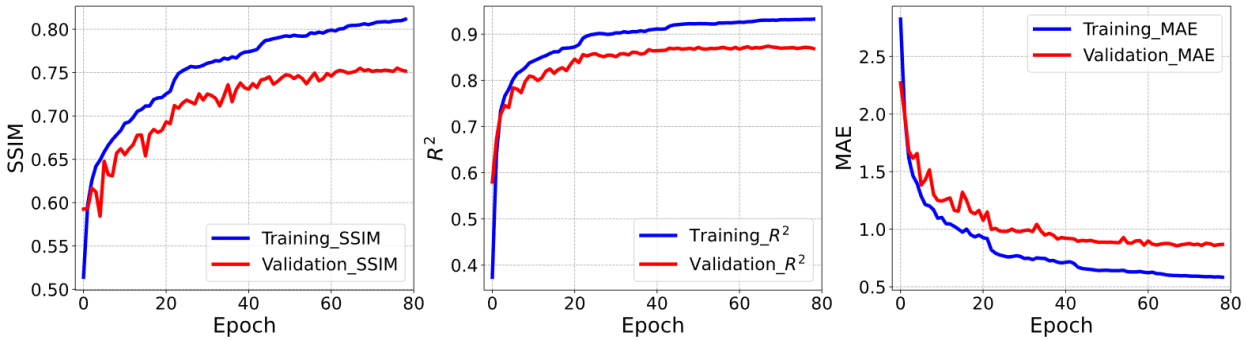

Fig. 15 SSIM, R^2, and MAE over epochs during the fine-tuning process on the training and validation sets

The collapse due to structural failure was simulated using the BCB tool. Fig. 16 shows the 3D model of the collapsed structure and two selected locations. The permittivity maps for the two locations were extracted and fed into the gprMax simulator to generate corresponding radargrams.

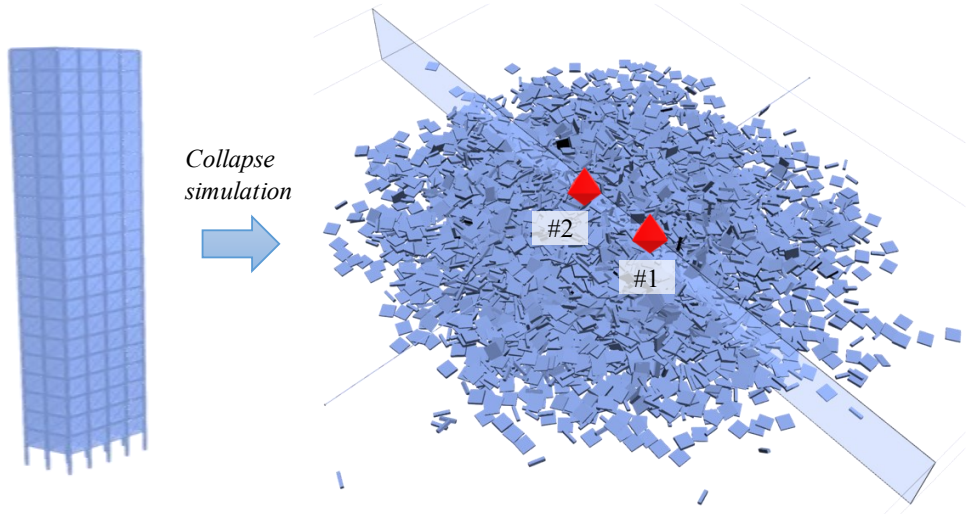

Fig. 16 3D model of the collapsed structure and target GPR survey locations for the simulated tall building collapse

Fig. 17 shows CycleGAN-augmented radargrams and ground-truth permittivity maps in the time-depth domain of target locations #1 and #2 shown in Fig. 16. The radargrams were fed into the inversion network to predict permittivity maps. The results indicate that the predicted permittivity map can point out large void spaces as highlighted by the black boxes. This can be viewed as an indicator of the generalization ability of the proposed method. However, it should also be noted that the model's performance on simulated collapsed buildings is worse compared to its results on the synthetic dataset. This is because a realistic building collapse could be more complex than a structural collapse generated by the random collapse generator with random parameters, such as the number of layers, subsurface void shape, size, and location. The performance on realistic building collapses can be improved by integrating prior knowledge regarding real collapse structure features in the collapse structure generation stage. Specifically, building collapses can be categorized into one of five patterns: lean-to, V-shape, pancake, cantilever floor, and A-frame. Each type of collapse is associated with the type of voids

formed underneath, which is critical for first responders to determine suitable operations. The characteristics of different types of collapses could be incorporated into the structural collapse simulation in the future to improve the model's performance in real-world applications.

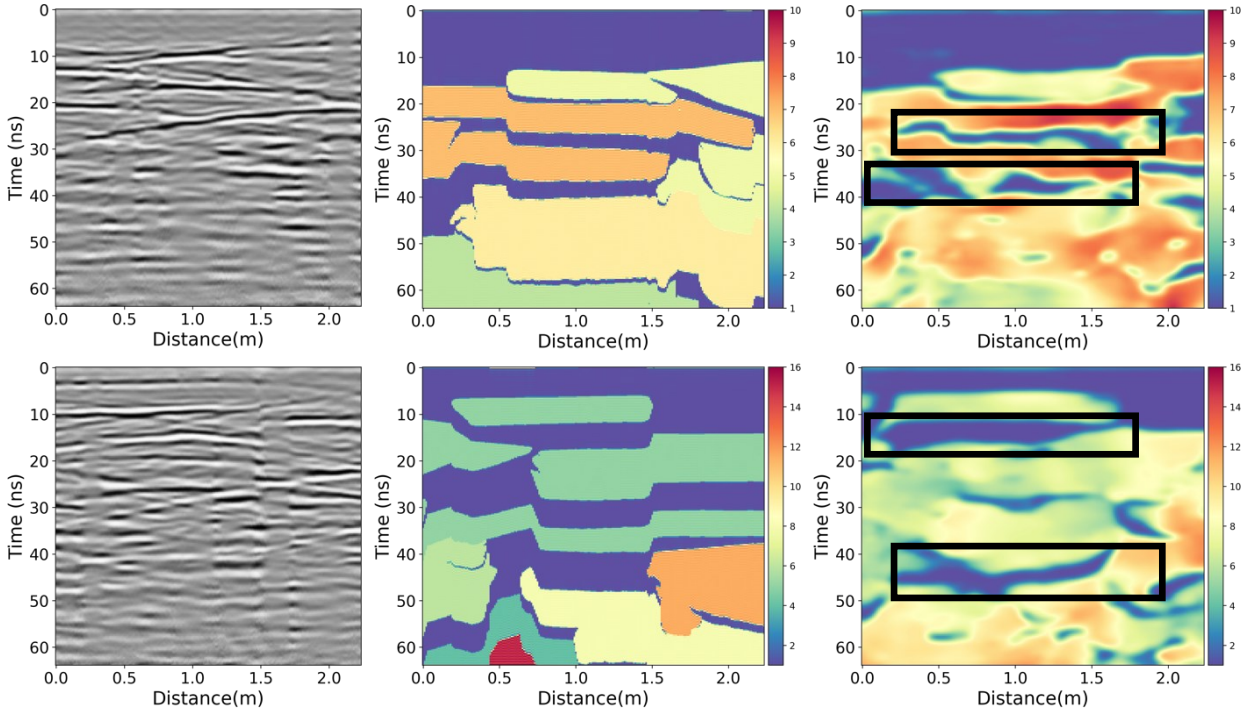

Fig. 17 Inversion results of the radargrams collected at locations #1 and #2. The first row is for location #1, and the second row is for location #2.

6.3 Applicability and contribution

The proposed method achieved an R^2 value of 0.76, an SSIM of 0.89, and an MAE of 1.49 in inferring the material permittivity from augmented radargrams. The inference time of the network is around 8 ms for a single radargram using NVIDIA Quadro P5000. The promising performance of our method demonstrates its potential to be applied to search-and-rescue operations. The proposed method was validated in simulations of a multistory apartment collapse and a tall building collapse, which produced complex and realistic collapsed structures. The predicted permittivity map can point out large void spaces, which can provide actionable information for search-and-rescue operations. Current practices for locating buried survivors consist of physical void searching, audible callouts, infrared/thermal imaging, electronic listening devices, and canine searching. The proposed method could be a great complement to current search-and-rescue practices by pointing out potential survivable spaces for victims. Furthermore, the proposed method can be integrated with existing robot platforms to survey disaster areas. For instance, GPR can be mounted on unmanned aerial vehicles (UAVs) such as DJI Matrice 600 to scan over uneven and heterogeneous structural collapses. The UAVs offer enough speed and flight time to cover a large disaster area. The network could be integrated into the onboard computers of UAVs to achieve nearly real-time inversion given the fast inference time of the network. The inversion results could also be leveraged to optimize scanning trajectory and parameters to map 3D subsurface structures.

This study contributes to the body of knowledge in two aspects. First, to address the lack of training data with correct labels, synthetic radargrams were generated from simulated scenarios of collapsed structures. The CycleGAN network was applied to reduce the domain gap between synthetic and real radargrams and augment the realism of synthetic radargrams for training, providing a new mechanism for preparing and augmenting data that are difficult to collect during disasters. The augmented radargrams can then be used to train the GPR inversion network, thus not only improving the capability of the network for inferring a large number of complex scenarios but also the scalability of the deep learning methods to real GPR data. Second, instead of detecting and segmenting nonintuitive features in GPR radargrams, a new DNN-based inversion network based on an encoder-decoder structure was trained using the augmented GPR radargrams to directly reconstruct permittivity maps corresponding to the cross-sections of collapsed structures. The Atrous Spatial Pyramid Pooling (ASPP) module was integrated into the network to capture neighboring GPR trace information in different scales by varying dilation rates. This paper offers a new method for complex and nonintuitive GPR data processing, particularly in time-critical missions. Moving beyond current techniques, the proposed method can rapidly process a large amount of nonintuitive GPR radargrams, reconstruct the interior scenarios, and infer important regions from the material permittivity such as void spaces in rubble, providing the interior layouts of collapsed structures to first responders and improving the effectiveness, efficiency, and safety of current search-and-rescue practices.

6.4 Limitations and future research

This study suffers from several limitations that deserve future study. Given the unavailability of field GPR data and its corresponding permittivity map, this study is focused on demonstrating the feasibility of the inversion network using collapsed structures simulated with a building collapse engine. The performance of the network in real disaster sites with complex collapsed structures remains to be evaluated. Therefore, in the future, extensive experiments should be conducted to test if the network can correctly reconstruct the interior models of collapsed structures at disaster sites. Second, while the permittivity map can provide critical information regarding interior scenarios such as survivable void spaces, materials of structures remain unexplored. Materials of subsurface structures are important for emergency responders to designate appropriate rescue strategies to reach potential trapped victims. For instance, concrete typically requires a greater effort to remove compared to wood. Therefore, future study is needed to obtain information on subsurface structure materials from GPR data with advanced algorithms. Third, the building collapse simulation was conducted using the BCB tool. The BCB is open-source software, which is well-maintained and can be accessed by practitioners in urban search-and-rescue organizations. It should also be noted that more-advanced physics engines are available, such as Extreme Loading for Structure (ELS) and Abaqus software. These advanced simulators have the potential to generate more realistic structural collapse simulations. Furthermore, using collapse simulators to create different types of structural collapse scenarios and generate a large amount of GPR data to train the inversion network is a promising research direction.

7. Conclusions

Significant efforts are needed to search for and rescue victims trapped in collapsed structures after natural and man-made disasters such as earthquakes, hurricanes, and explosions. Knowledge of the interiors of collapsed structures is not made available to first responders by existing techniques, hindering efficient, effective, and safe search-and-rescue operations. To address this urgent need, this paper proposed a DNN-based GPR data inversion approach to

reconstruct permittivity maps, which can be used to infer the interiors of collapsed structures. A large amount of synthetic GPR radargrams with ground-truth permittivity maps were simulated and augmented using the CycleGAN network to improve the realism of the synthetic radargrams. A DNN-based inversion network was designed based on an encoder-decoder structure and trained using the augmented radargrams to reconstruct permittivity maps corresponding to the cross-sections of collapsed structures. The result of the visual Turing test indicated that the realism of augmented radargrams is substantially improved using the GAN. Notably, the proportion of augmented radargrams misjudged as "Real" was 27.3%, which is even higher than the proportion of real radargrams judged as "Real" (22.7%). The proposed inversion method achieved an R^2 value of 0.93, an MAE of 0.73, and an SSIM of 0.95 in inferring the material permittivity of collapsed structures from synthetic radargrams. Furthermore, the predicted permittivity map was used to infer voids, achieving an F1 score of 64.34%, a precision of 63.06%, and a recall of 71.84% at the pixel level. On the augmented radargrams, the network achieved an R^2 value of 0.76, an MAE of 1.49, and an SSIM of 0.89 in predicting the permittivity map. The void detection on augmented radargrams achieved an F1 score of 45.2%, a precision of 45.35%, and a recall of 53.99% at the pixel level. The proposed GPR inversion network in reconstructing subsurface permittivity maps was further validated on two collapsed multistory structures simulated using a building collapse simulator.

Acknowledgement

This research was funded by the National Science Foundation (NSF) via the Grants #1850008, #2129003, and the Tennessee Department of Transportation (TDOT) via the Research Project RES2021-05: "Drones and Other Technologies to Assist in Disaster Relief Efforts". The authors gratefully acknowledge the support. Any opinions, findings, recommendations, and conclusions in this paper are those of the authors, and do not necessarily reflect the views of NSF, TDOT, the University of Tennessee, Knoxville, and the University of Hong Kong.

References

[1] M. Statheropoulos, A. Agapiou, G.C. Pallis, K. Mikedi, S. Karma, J. Vamvakari, M. Dandoulaki, F. Andritsos, C.L.P. Thomas, Factors that affect rescue time in urban search and rescue (USAR) operations, Natural Hazards. 75 (2015) pp. 57–69. https://doi.org/10.1007/s11069-014-1304-3.

[2] R.R. Murphy, J. Casper, M. Micire, Potential tasks and research issues for mobile robots in roboCup rescue, in: Springer, Berlin, Heidelberg, 2001: pp. 339–344. https://doi.org/10.1007/3-540-45324-5_36.

[3] S. Gorman, Final death toll from Florida condominium collapse put at 98, (2021). https://www.reuters.com/world/us/final-death-toll-florida-condominium-collapse-put-98-2021-07-26/ (accessed October 16, 2021).

[4] J. Thompson, M. Rehn, H.M. Lossius, D. Lockey, Risks to emergency medical responders at terrorist incidents: a narrative review of the medical literature, Critical Care. 18 (2014) pp. 1–10. https://doi.org/10.1186/s13054-014-0521-1.

[5] D.B. Cist, Non-destructive evaluation after destruction: using ground penetrating radar for search and rescue, in: 7th International Symposium on Non-Destructive Testing in Civil Engineering, Nantes, France, 2009.

[6] D. Hu, S. Li, J. Chen, V.R. Kamat, Detecting, locating, and characterizing voids in disaster rubble for search and rescue, Advanced Engineering Informatics. 42 (2019) pp. 100974. https://doi.org/10.1016/j.aei.2019.100974.

[7] D. Goodman, S. Piro, GPR remote sensing in archaeology, Springer Berlin Heidelberg, Berlin, Heidelberg, 2013. https://doi.org/10.1007/978-3-642-31857-3.
[8] C.A. Grosvenor, R.T. Johnk, J. Baker-Jarvis, M.D. Janezic, B. Riddle, Time-domain free-field measurements of the relative permittivity of building materials, IEEE Transactions on Instrumentation and Measurement. 58 (2009) pp. 2275–2282. https://doi.org/10.1109/TIM.2009.2013916.
[9] B. Liu, Y. Ren, H. Liu, H. Xu, Z. Wang, A.G. Cohn, P. Jiang, GPRInvNet: deep learning-based Ground-Penetrating Radar data inversion for tunnel linings, IEEE Transactions on Geoscience and Remote Sensing. 59 (2021) pp. 8305–8325. https://doi.org/10.1109/TGRS.2020.3046454.
[10] Y. Ji, F. Zhang, J. Wang, Z. Wang, P. Jiang, H. Liu, Q. Sui, Deep neural network-based permittivity inversions for Ground Penetrating Radar data, IEEE Sensors Journal. 21 (2021) pp. 8172–8183. https://doi.org/10.1109/JSEN.2021.3050618.
[11] S. Li, H. Cai, V.R. Kamat, Uncertainty-aware geospatial system for mapping and visualizing underground utilities, Automation in Construction. 53 (2015) pp. 105–119. https://doi.org/10.1016/j.autcon.2015.03.011.
[12] S. Li, H. Cai, D.M. Abraham, P. Mao, Estimating features of underground utilities: hybrid GPR/GPS approach, Journal of Computing in Civil Engineering. 30 (2014) pp. 04014108. https://doi.org/10.1061/(asce)cp.1943-5487.0000443.
[13] J. Feng, L. Yang, E. Hoxha, D. Sanakov, S. Sotnikov, J. Xiao, GPR-based Model Reconstruction System for Underground Utilities Using GPRNet, in: 2021 IEEE International Conference on Robotics and Automation (ICRA), IEEE, 2021: pp. 845–851. https://doi.org/10.1109/ICRA48506.2021.9561355.
[14] G. Kouros, I. Kotavelis, E. Skartados, D. Giakoumis, D. Tzovaras, A. Simi, G. Manacorda, 3D underground mapping with a mobile robot and a GPR antenna, in: 2018 IEEE/RSJ International Conference on Intelligent Robots and Systems (IROS), IEEE, 2018: pp. 3218–3224. https://doi.org/10.1109/IROS.2018.8593848.
[15] Z. Tong, J. Gao, H. Zhang, Recognition, location, measurement, and 3D reconstruction of concealed cracks using convolutional neural networks, Construction and Building Materials. 146 (2017) pp. 775–787. https://doi.org/10.1016/j.conbuildmat.2017.04.097.
[16] H.U. Levatti, P.C. Prat, A. Ledesma, A. Cuadrado, J.A. Cordero, Experimental analysis of 3D cracking in drying soils using Ground-Penetrating Radar, Geotechnical Testing Journal. 40 (2017) pp. 20160066. https://doi.org/10.1520/GTJ20160066.
[17] D. Hu, F. Hou, S. Li, Ground-penetrating radar-based root architecture detection and characterization, in: 18th International Conference on Ground Penetrating Radar, 2020: pp. 243–246. https://doi.org/10.1190/gpr2020-065.1.
[18] X. Liu, J. Chen, J.R. Butnor, G. Qin, X. Cui, B. Fan, H. Lin, L. Guo, Noninvasive 2D and 3D mapping of root zone soil moisture through the detection of coarse roots with Ground-Penetrating Radar, Water Resources Research. 56 (2020) pp. e2019WR026930. https://doi.org/10.1029/2019WR026930.
[19] D. Hu, F. Hou, J. Blakely, S. Li, Augmented reality based visualization for concrete bridge deck deterioration characterized by Ground Penetrating Radar, in: Construction Research Congress 2020: Computer Applications, 2020: pp. 1156–1164. https://doi.org/10.1061/9780784482865.122.
[20] A. Instanes, I. Lønne, K. Sandaker, Location of avalanche victims with ground-penetrating radar, Cold Regions Science and Technology. 38 (2004) pp. 55–61. https://doi.org/10.1016/j.coldregions.2003.08.002.

[21] A. Heilig, M. Schneebeli, W. Fellin, Feasibility study of a system for airborne detection of avalanche victims with ground penetrating radar and a possible automatic location algorithm, Cold Regions Science and Technology. 51 (2008) pp. 178–190. https://doi.org/10.1016/j.coldregions.2007.06.003.
[22] F. Fruehauf, A. Heilig, M. Schneebeli, W. Fellin, O. Scherzer, Experiments and algorithms to detect snow avalanche victims using airborne ground-penetrating radar, IEEE Transactions on Geoscience and Remote Sensing. 47 (2009) pp. 2240–2251. https://doi.org/10.1109/TGRS.2009.2012717.
[23] N. Diamanti, A.P. Annan, I. Giannakis, Predicting GPR performance for buried victim search & rescue, in: 2016 16th International Conference on Ground Penetrating Radar (GPR), IEEE, 2016: pp. 1–6. https://doi.org/10.1109/ICGPR.2016.7572642.
[24] D. Yang, Z. Zhu, B. Liang, Vital sign signal extraction method based on permutation entropy and EEMD algorithm for Ultra-Wideband Radar, IEEE Access. 7 (2019) pp. 178879–178890. https://doi.org/10.1109/ACCESS.2019.2958600.
[25] K. Yan, S. Wu, G. Fang, Detection of quasi-static trapped human being using mono-static UWB life-detection radar, Applied Sciences. 11 (2021) pp. 3129. https://doi.org/10.3390/app11073129.
[26] J. Chen, S. Li, D. Liu, X. Li, AiRobSim: simulating a multisensor aerial robot for urban search and rescue operation and training, Sensors. 20 (2020) pp. 5223. https://doi.org/10.3390/s20185223.
[27] D. Hu, S. Li, 3D reconstruction of voids in disaster rubble using ground-penetrating radar, in: 18th International Conference on Ground Penetrating Radar, Golden, Colorado, 14–19 June 2020, Society of Exploration Geophysicists, Golder, Colorado, 2020: pp. 452–455. https://doi.org/10.1190/gpr2020-117.1.
[28] D. Hu, L. Chen, J. Du, J. Cai, S. Li, See through Disaster Rubble in 3D with Ground Penetrating Radar and Interactive Augmented Reality for Urban Search and Rescue, Journal of Computing in Civil Engineering. (2022). https://doi.org/10.1061/(ASCE)CP.1943-5487.0001038.
[29] Independent Advisory Group on Non-Ionising Radiation, Health effects from radiofrequency electromagnetic fields, 2012. https://assets.publishing.service.gov.uk/government/uploads/system/uploads/attachment_data/file/333080/RCE-20_Health_Effects_RF_Electromagnetic_fields.pdf (accessed April 5, 2022).
[30] R. Persico, L. Pajewski, Safety issues in ground-penetrating radar and near-surface geophysical prospecting, in: 2016 24th International Conference on Software, Telecommunications and Computer Networks (SoftCOM), IEEE, 2016. https://doi.org/10.1109/SOFTCOM.2016.7772178.
[31] R. Persico, A. Provenzano, C. Trela, M. Sato, K. Takahashi, S. Arcone, S. Koppenjan, L. Stolarczyk, E.C. Utsi, S. Ebihara, Recommendations for the safety of people and instruments in Ground-Penetrating Radar and near-surface geophysical prospecting, European Association of Geoscientists & Engineers, Hague, 20159462821623.
[32] Z.W. Wang, M. Zhou, G.G. Slabaugh, J. Zhai, T. Fang, Automatic detection of bridge deck condition from ground penetrating radar images, IEEE Transactions on Automation Science and Engineering. 8 (2011) pp. 633–640. https://doi.org/10.1109/TASE.2010.2092428.
[33] R. Ahmadi, N. Fathianpour, Estimating geometrical parameters of cylindrical targets detected by ground-penetrating radar using template matching algorithm, Arabian Journal of Geosciences. 10 (2017) pp. 140. https://doi.org/10.1007/s12517-017-2901-8.

[34] K. Dinh, N. Gucunski, T.H. Duong, Migration-based automated rebar picking for condition assessment of concrete bridge decks with ground penetrating radar, NDT and E International. 98 (2018) pp. 45–54. https://doi.org/10.1016/j.ndteint.2018.04.009.
[35] H. Qin, X. Xie, J.A. Vrugt, K. Zeng, G. Hong, Underground structure defect detection and reconstruction using crosshole GPR and Bayesian waveform inversion, Automation in Construction. 68 (2016) pp. 156–169. https://doi.org/10.1016/j.autcon.2016.03.011.
[36] D. Feng, X. Wang, B. Zhang, Improving reconstruction of tunnel lining defects from ground-penetrating radar profiles by multi-scale inversion and bi-parametric full-waveform inversion, Advanced Engineering Informatics. 41 (2019) pp. 100931. https://doi.org/10.1016/J.AEI.2019.100931.
[37] J. Zhang, S. Ye, L. Yi, Y. Lin, H. Liu, G. Fang, A hybrid method applied to improve the ffficiency of full-waveform inversion for pavement characterization, Sensors. 18 (2018) pp. 2916. https://doi.org/10.3390/s18092916.
[38] P. Kaur, K.J. Dana, F.A. Romero, N. Gucunski, Automated GPR rebar analysis for robotic bridge deck evaluation, IEEE Transactions on Cybernetics. 46 (2016) pp. 2265–2276. https://doi.org/10.1109/TCYB.2015.2474747.
[39] H. Harkat, A.E. Ruano, M.G. Ruano, S.D. Bennani, GPR target detection using a neural network classifier designed by a multi-objective genetic algorithm, Applied Soft Computing. 79 (2019) pp. 310–325. https://doi.org/10.1016/j.asoc.2019.03.030.
[40] I. Giannakis, A. Giannopoulos, C. Warren, A machine learning scheme for estimating the diameter of reinforcing bars using Ground Penetrating Radar, IEEE Geoscience and Remote Sensing Letters. 18 (2021) pp. 461–465. https://doi.org/10.1109/LGRS.2020.2977505.
[41] F. Hou, W. Lei, S. Li, J. Xi, M. Xu, J. Luo, Improved Mask R-CNN with distance guided intersection over union for GPR signature detection and segmentation, Automation in Construction. 121 (2021) pp. 103414. https://doi.org/10.1016/j.autcon.2020.103414.
[42] K. Dinh, N. Gucunski, T.H. Duong, An algorithm for automatic localization and detection of rebars from GPR data of concrete bridge decks, Automation in Construction. 89 (2018) pp. 292–298. https://doi.org/10.1016/J.AUTCON.2018.02.017.
[43] C. Warren, A. Giannopoulos, I. Giannakis, gprMax: Open source software to simulate electromagnetic wave propagation for Ground Penetrating Radar, Computer Physics Communications. 209 (2016) pp. 163–170. https://doi.org/10.1016/j.cpc.2016.08.020.
[44] O. Ronneberger, P. Fischer, T. Brox, U-net: Convolutional networks for biomedical image segmentation, in: International Conference on Medical Image Computing and Computer-Assisted Intervention, Springer Verlag, 2015: pp. 234–241. https://doi.org/10.1007/978-3-319-24574-4_28.
[45] J.-Y. Zhu, T. Park, P. Isola, A.A. Efros, Unpaired image-to-image translation using cycle-consistent adversarial networks, in: 2017 IEEE International Conference on Computer Vision (ICCV), IEEE, 2017: pp. 2223–2232. https://doi.org/10.1109/ICCV.2017.244.
[46] J. Chen, S. Li, D. Liu, W. Lu, Indoor camera pose estimation via style-transfer 3D models, Computer-Aided Civil and Infrastructure Engineering. 37 (2022) pp. 335–353. https://doi.org/10.1111/mice.12714.
[47] A. Paszke, S. Gross, F. Massa, A. Lerer, J. Bradbury, G. Chanan, T. Killeen, Z. Lin, N. Gimelshein, L. Antiga, Pytorch: An imperative style, high-performance deep learning library, Adv Neural Inf Process Syst. 32 (2019) pp. 8026–8037.
[48] Z. Wang, E.P. Simoncelli, A.C. Bovik, Multiscale structural similarity for image quality assessment, in: The Thrity-Seventh Asilomar Conference on Signals, Systems &

Computers, 2003, IEEE, 2003: pp. 1398–1402. https://doi.org/10.1109/ACSSC.2003.1292216.
[49] Y. Gal, Z. Ghahramani, Dropout as a bayesian approximation: Representing model uncertainty in deep learning, in: Proceedings of the 33rd International Conference on International Conference on Machine Learning, JMLR.org, 2016: pp. 1050–1059.
[50] O. Walte, K. Kostack, Blender and Bullet physics engine based on fast on-site assessment tool, Uusimaa, 2017. https://inachuslaurea.files.wordpress.com/2021/07/inachus_d3.5_luas_v1.0.pdf (accessed April 5, 2022).
[51] T. Bloch, R. Sacks, O. Rabinovitch, Interior models of earthquake damaged buildings for search and rescue, Advanced Engineering Informatics. 30 (2016) pp. 65–76. https://doi.org/10.1016/j.aei.2015.12.001.
[52] H. Maeda, T. Kashiyama, Y. Sekimoto, T. Seto, H. Omata, Generative adversarial network for road damage detection, Computer-Aided Civil and Infrastructure Engineering. 36 (2021) pp. 47–60. https://doi.org/10.1111/mice.12561.
[53] Z. Xiang, G. Ou, A. Rashidi, Robust cascaded frequency filters to recognize rebar in GPR data with complex signal interference, Automation in Construction. 124 (2021) pp. 103593. https://doi.org/10.1016/j.autcon.2021.103593.
[54] J. Feng, L. Yang, H. Wang, Y. Tian, J. Xiao, Subsurface pipes detection using DNN-based back projection on GPR data, in: 2021 IEEE Winter Conference on Applications of Computer Vision (WACV), IEEE, 2021: pp. 266–275. https://doi.org/10.1109/WACV48630.2021.00031.